Joint space aspect reconstruction of wide-angle SAR exploiting sparsity

Ivana Stojanovic[a], Mujdat Cetin[b], William C. Karl[c]

[a,c]ECE Department, Boston University, Boston, USA
[b]Sabanci University, Istanbul, Turkey

ABSTRACT

In this paper we present an algorithm for wide-angle synthetic aperture radar (SAR) image formation. Reconstruction of wide-angle SAR holds a promise of higher resolution and better information about a scene, but it also poses a number of challenges when compared to the traditional narrow-angle SAR. Most prominently, the isotropic point scattering model is no longer valid. We present an algorithm capable of producing high resolution reflectivity maps in both space and aspect, thus accounting for the anisotropic scattering behavior of targets. We pose the problem as a non-parametric three-dimensional inversion problem, with two constraints: magnitudes of the backscattered power are highly correlated across closely spaced look angles and the backscattered power originates from a small set of point scatterers. This approach considers jointly all scatterers in the scene across all azimuths, and exploits the sparsity of the underlying scattering field. We implement the algorithm and present reconstruction results on realistic data obtained from the XPatch Backhoe dataset.

Keywords: SAR, wide-angle, sparse measurements, edge-preserving regularization

1. INTRODUCTION

Wide-angle SAR (WSAR), where radar returns are collected over a large range of angles, holds the promise of increased spatial resolution. However, in collecting data over such a large angular range a number of the assumptions used in standard, narrow-angle SAR are violated. In particular, the common assumption that target reflectivity is only a function of spatial location, and not aspect, is no longer a good approximation to reality. Over large angular extents the energy reflected by targets is, in general, not uniform and most targets exhibit only limited scattering persistence.[1]

As a result, standard Fourier-based SAR image formation algorithms, such as the polar-format algorithm, perform poorly. The resulting imagery produced by these methods have limited resolution and display confounding artifacts.[2] Overall, these methods fail to completely realize the potential of WSAR.

Wide angle SAR reconstruction has been addressed in several papers. In one work, WSAR is approached as a collection of multiple overlapping 20° sub-apertures and reflectivity functions in each sub-aperture are independently reconstruct via the conventional polar-format algorithm or point-enhanced l_p norm regularization.[2] Alternatively, the problem is approached as a sparse, inverse problem over an overcomplete dictionary, with a dictionary element representing a prescribed reflectivity signature of a spatial pixel along the azimuth direction.[3]

In this paper, we also consider a spotlight synthetic aperture radar system (SAR)[4] with collocated transmitter and receiver operating in a monostatic configuration over a large angular range. Similar to the overcomplete dictionary approach,[3] we explicitly model the anisotropy of the target scattering behavior and estimate the angle-dependent scattering behavior at each scatter location. In contrast to previous approaches, however, we approach the problem as a direct, non-parametric reconstruction of the entire three-dimensional angle-dependent scattering field. We exploit the correlations in target reflectivity in aspect and the spatial sparsity of target scattering by including priors on this behavior in the reconstruction process. This approach does not require detailed prior knowledge of scatter type, yet can successfully focus information in the data. In addition, this approach provides robustness to data loss, allowing preservation of image quality from reduced data.

The rest of the paper is organized as follows. In Section 2 we outline the basic spotlight SAR scattering physics and present the anisotropic forward scattering model we use. Section 3 outlines our inverse problem formulation and finally Section 4 gives image reconstruction results obtained by the algorithm.

2. FORWARD MODEL

Typical assumption for narrow synthetic apertures is that the reflectivity of a given spatial differential area is isotropic. While this is a reasonable assumption for narrow apertures of a few degrees, most of the scene's scatterers exhibit anisotropic response when viewed over large aspects. In contrast to isotropic scattering where the reflectivity function is a function of spatial variables (x_p, y_p), in the general case, the reflectivity is additionally dependent on the aspect angle. A backscattered signal $r_{(x_p,y_p)}(t,\theta)$ of a spatial differential area centered at (x_p, y_p) to a pulse $\gamma(t)$ transmitted at time t, with the aircraft at an aspect θ is a delayed transmitted pulse modulated by the area's anisotropic reflectivity function $s(x_p, y_p, \theta)$. Mathematically, the backscattered signal is described by the following equation:

$$r_{(x_p,y_p)}(t,\theta) = \Re \left\{ A(x_p,y_p,\theta)s(x_p,y_p;\theta)\gamma\left(t - 2\frac{R_p(\theta)}{c}\right) \right\} dxdy,$$

where $R_p(\theta)$ is the distance from the differential area $dxdy$ to the aircraft location at the aspect θ. The factor $A(x_p,y_p,\theta)$ accounts for propagation attenuation, transmitter and receiver antenna beam patterns, etc. This factor can be safely ignored, i.e. assumed to be a constant, when the scene extent is much smaller compared to the aircraft's stand-off range and when transmit and receive antenna beampatterns are omnidirectional. Again, typical isotropic point scattering assumption is relaxed in order to account for limited reflectivity persistence over wide aspect angles.

Now, to characterize a return from a realistic complex scene, a typical set of operating assumptions are put in place. When the impinging signal wavelength is small relative to the target extent, the overall response of a complex scene is well approximated as a superposition of a set of the scene's differential scatterers. Under the single-scattering (Born) approximation there is no interaction of scene components. Assuming that the transmitted waveform is a chirp pulse $\gamma(t) = e^{j(2\pi f_c t + \alpha t^2)}$ with center frequency f_c and rate α limited to time $-\frac{T}{2} \le t \le \frac{T}{2}$, the received signal, after pre-processing steps of downconversion and matched filtering, is as follows:

$$r(t,\theta) = \int\int_{x^2+y^2\le L} s(x,y;\theta)e^{-j\Omega(t)(x\cos(\theta)+y\sin(\theta))}dxdy, \tag{1}$$

with the spatial frequency variable $\Omega(t) = \frac{2}{c}(2\pi f_c + 2\alpha(t - \frac{2R_c}{c}))$. In the discrete world, the backscattered signal collected at discrete look angles θ_s is sampled at times t_s to allow digital signal processing. In the time interval of interest the spatial frequency $\Omega(t)$ varies in the range $\left(\frac{2\pi}{c}f_c - \frac{\alpha T}{2}, \frac{2\pi}{c}f_c + \frac{\alpha T}{2}\right)$. Typically, the time sampling points t_s are chosen such that spatial discrete frequencies $\Omega(t_s) = \frac{4\pi}{c}f_s$ cover the whole range uniformly. Assuming that the scene under surveillance consists of multitude of point scatterers at locations (x_p, y_p), the
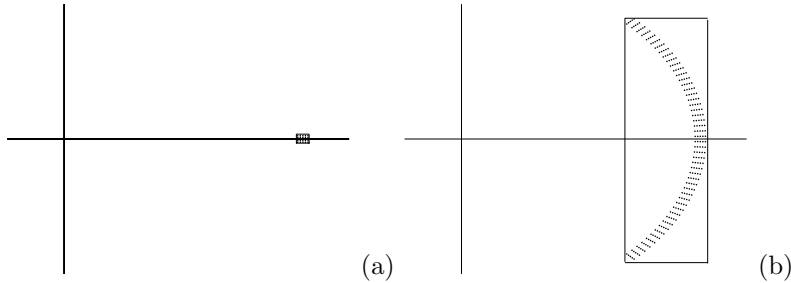

Figure 1. SAR spatial frequency support region at the center frequency $f_c = 10$ GHz: (a) narrow-band, narrow-angle case ($B = 0.5$GHz, $\Delta\theta = 5^o$) and (b) narrow-band, wide-angle ($B = 0.5$GHz, $\Delta\theta = 90^o$).

received signal can be written in discrete form as:

$$r(f_s,\theta_s) = \sum_p s(x_p,y_p;\theta_s)e^{-j\frac{4\pi f_s}{c}(x_p\cos(\theta_s)+y_p\sin(\theta_s))},$$

at a discrete frequency f_s within bandwidth B and at a discrete aspect θ_s within an aperture of the extent $\Delta\theta$, with $r(f_s, \theta_s)$ being commonly referred to as phase history. Note that the point scatterer model derived above is the discrete approximation of the continuous superposition principle that relates phase history data to continuous reflectivity field through the integral Equation 1.

Contrast between the spatial frequency support of the narrow-angle and wide-angle data collection is presented in Figure 1. Due to the circular arch shape of the spatial frequency support, traditional polar format algorithm is expected to perform poorly in the wide-angle collection scenario. Wide-angle problem is ill-posed, and direct inversion techniques result in a number of artifacts. In the following section we outline our approach that aims at joint space-aspect reconstruction of a scene viewed from wide aspect angles.

3. IMAGE FORMATION

We first define a wide angle SAR image as a set of aspect dependent spatial images. Due to the dependence of the reflectivity response on the aspect of an impinging electromagnetic wave, there exists a reflectivity map of a scene at each aspect. Assume that the ground scene is interrogated and reconstructed at a number of different aspects, I. Denote the set of time observations at the aspect θ_i as $\mathbf{r}_{\theta_i}$ and denote the spatial reflectivity field at the aspect θ_i, as $\mathbf{s}_{\theta_i}$. In the discrete representation, at each aspect angle, Equation 1 reduces to a linear system of equations of the form $\mathbf{r}_{\theta_i} = \mathbf{\Phi}_{\theta_i}\mathbf{s}_{\theta_i}$, where $\mathbf{\Phi}_{\theta_i}$ is the discrete representation of the SAR forward operator. Overall we can write:

$$
\begin{bmatrix} \mathbf{r}_{\theta_1} \\ \mathbf{r}_{\theta_2} \\ \vdots \\ \mathbf{r}_{\theta_I} \end{bmatrix} = \begin{bmatrix} \mathbf{\Phi}_{\theta_1} & \mathbf{0} & \dots & \mathbf{0} \\ \mathbf{0} & \mathbf{\Phi}_{\theta_2} & \dots & \mathbf{0} \\ \vdots & \vdots & \vdots & \vdots \\ \mathbf{0} & \dots & \mathbf{0} & \mathbf{\Phi}_{\theta_I} \end{bmatrix} \begin{bmatrix} \mathbf{s}_{\theta_1} \\ \mathbf{s}_{\theta_2} \\ \vdots \\ \mathbf{s}_{\theta_I} \end{bmatrix} + \mathbf{z}.
\tag{2}
$$

We can represent this relationship compactly as follows:

$$
\mathbf{r} = \mathbf{\Phi}\mathbf{s} + \mathbf{z}
\tag{3}
$$

where $\mathbf{z}$ is a random unknown vector modeling additive system noise, as well as any model mismatch errors.

Note that two comments are in order for the above set of equations. First, the equations represent in essence a set of I independent systems of linear equations. Thus, hopes of any joint processing can not come from the forward observation model, but rather from some sort of prior information that we have about the unknown reflectivity field that we seek to reconstruct. Second, each individual problem $\mathbf{r}_{\theta_i} = \mathbf{\Phi}_{\theta_i}\mathbf{s}_{\theta_i}$ is ill-conditioned. The ill-conditioned discrete problems pose several issues in their own right, and typically some sort of prior information is utilized to aid solution stabilization and potentially reduce non-observability of components that lie in the null space of the forward operator.[5]

Under the point scattering assumption, the spatial reflectivity field at aspect i, $\mathbf{s}_{\theta_i}$, is well modeled as a spatially sparse set of reflectivity centers. Additionally, each point scatterer has a limited persistence over azimuth, but within its persistence there exist a high correlation between scatterer magnitude responses to excitations at closely spaced observation aspects. Combining these observations together, the reflectivity image magnitudes $|\mathbf{s}_{\theta_i}|$ at discrete aspects $i = \{1, \dots, I\}$ should be highly correlated, and yet allow for abrupt changes in reflectivity on a subset of scatterers. Thus, in our reconstruction algorithm we seek to impose smoothness on the point scatterer's response in the azimuth direction, and sparsity across point scatterers in the spatial domain.

To form an image we take a cost or energy minimization approach, wherein we combine the physical observation model in (2) with a term capturing prior information:

$$
\hat{\mathbf{s}} = \arg\min_{\mathbf{s}} J_{data}(\mathbf{r}, \mathbf{s}) + J_{prior}(\mathbf{s}).
\tag{4}
$$

For the data-fidelity term $J_{data}(\mathbf{r}, \mathbf{s})$ we use the standard least square penalty, $J_{data}(\mathbf{r}, \mathbf{s}) = \|\mathbf{r} - \mathbf{\Phi}\mathbf{s}\|_2^2$.

We can capture the correlation in azimuth by penalizing the p-norm of the change in scattering magnitude at each pixel from angle to angle. We can capture the spatial sparsity of scatterers by penalizing the q-norm of

the total energy across aspect at each pixel[6,7] . Denote the total number of pixels in a spatial image as N. We use the following functional for the prior penalty term reflecting these insights:

$$J_{prior}(\mathbf{s}) = \alpha \sum_{n=1}^{N} \sum_{i=1}^{I-1} ||s(x_n, y_n, \theta_{i+1})| - |s(x_n, y_n, \theta_i)||^p$$

$$+ \beta \sum_{n=1}^{N} \left[\sqrt{\sum_{i=1}^{I} |s(x_n, y_n, \theta_i)|^2} \right]^q . \tag{5}$$

Typically, we choose $p < 1$ and $q < 1$ to achieve desired sparsity[6,7] .

Note that both regularization terms are applied explicitly to magnitudes $|\mathbf{s}|$ of the complex reflectivity field $\mathbf{s}$. The second regularization term involves a l_2-norm computation which is naturally defined in terms of the magnitudes of the complex field. The first term is also expressed as the function of the field's magnitudes since it has been observed that the backscatter power is very similar across closely spaced look angles. Thus, the regularizing functional $J_{prior}(\mathbf{s})$ is non-linear function of real and imaginary parts of the field.

A solution to the inversion problem is obtained by minimizing the cost function of Equation 4. For the case when $p = q = 1$ the problem is convex and there exists a global, unique, solution. The minimization problem is in fact a second-order cone problem, that can be effectively solved by commercially available solvers. In the case when $p < 1$, $q < 1$, the convexity is lost and no local optimization algorithm can guarantee that it reaches the global minimum. Optimal sparsity is reached for $p = 0$, but the problem is then NP hard and prohibitively expensive for even moderate problem sizes. For $p,q < 1$ we use an iterative quasi-Newton method that is shown to work well on this class of problems.[8] An iterative algorithm used to find a minimizer of the cost function in Equation 4 is given in Appendix.

The computational complexity of the optimization problem in Equation 4 grows with the number of observation/reconstruction aspects. However, there is an inherit flexibility in the problem formulation, which allows for decoupling of the phase history collection aspects and the spatial field reconstruction aspects. This decoupling is carried through by mapping several azimuth returns to one spatial image. In other words, the anisotropic scattering assumption is relaxed to the isotropic within the small sub-aperture. Assume that $\{\theta_1, \ldots \theta_I\}$ now represent reconstruction aspects. At the reconstruction angle θ_i we now collect K azimuth returns, i.e. $\{\theta_i^1, \ldots \theta_i^K\}$. Thus,

$$\mathbf{r}_{\theta_i} = \begin{bmatrix} \mathbf{r}_{\theta_i^1} \\ \vdots \\ \mathbf{r}_{\theta_i^K} \end{bmatrix}, \quad \mathbf{\Phi}_{\theta_i} = \begin{bmatrix} \mathbf{\Phi}_{\theta_i^1} \\ \vdots \\ \mathbf{\Phi}_{\theta_i^K} \end{bmatrix}, \tag{6}$$

where $\mathbf{r}_{\theta_i^k}$ and $\mathbf{\Phi}_{\theta_i^k}$ are the discrete returned signal and the discrete forward SAR operator at the observation angle θ_i^k, respectively. The formality of the reconstruction algorithm in Equation 4 carries through unchanged with the new meaning assigned to $\mathbf{r}, \mathbf{\Phi}$ and $\mathbf{s}$.

Reduction of the number of reconstructed images poses a trade-off in between the computational complexity and the problem ill-conditioning on one side and a possible model mismatch on the other side. By assigning a small sub-aperture to each image, the degree of the ill-conditioning of a subproblem $\mathbf{r}_{\theta_i} = \mathbf{\Phi}_{\theta_i} \mathbf{s}_{\theta_i}$ is reduced by simply reducing a ratio of a number of measurements to a number unknowns. However, sub-aperture size should be chosen carefully to reduce the model mismatch. From empirical data, researchers[1] point out that the response remains isotropic, or approximately constant for aspect angles as large as 20°. Thus one could apply isotropic scattering on angular widths of a few degrees without considerably compromising the accuracy of the model.

We emphasize the spatial geometry of the data collection, as well as aspect angles at which the spatial reflectivity fields are being reconstructed on Figure 2. This figure shows a target in the coordinate center and the aircraft's circular trajectory at a large stand-off range, with phase history returns over small sub-apertures tied to one spatial image.
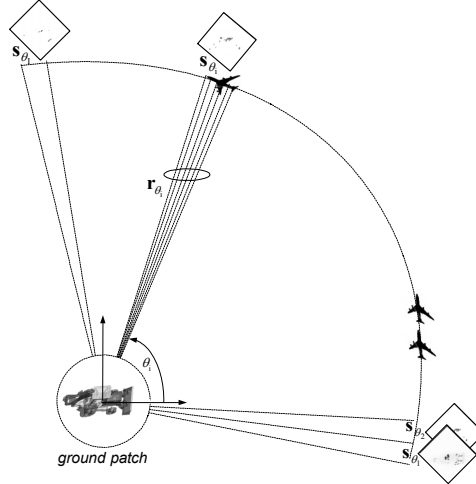
Figure 2. Wide-angle SAR data collection and reflectivity reconstruction geometry - the aircraft transmits pulses at the ground patch from a circular trajectory and reflectivity fields of the ground patch are reconstructed at a discrete set of aspects.

4. ALGORITHM ANALYSIS AND NUMERICAL SIMULATIONS

In this section we first analyze our algorithm on a synthetic data in order to derive some performance measures impossible to obtain without knowledge of the ground truth. In the second part of this section we show reflectivity field reconstructions obtained by applying the algorithm to the Backhoe dataset, generated with the XPatch simulator.[9] In both cases, we contrast joint reconstruction with independent, point enhanced processing,[2] obtained by minimizing the cost function $J(\mathbf{s}_{\theta_i}) = \|\mathbf{r}_{\theta_i} - \mathbf{\Phi}_{\theta_i}\mathbf{s}_{\theta_i}\|_2^2 + \beta\|\|\mathbf{s}_{\theta_i}\|\|_q^q$, $\forall i \in \{1, \ldots, I\}$, where $\mathbf{r}_{\theta_i}$ and $\mathbf{\Phi}_{\theta_i}$ are defined as before.

4.1 Performance metrics

In this section we outline performance measures used on experiments in a controlled environment to verify reconstruction abilities of our algorithm. Namely, we contrast the joint reconstruction to the point-enhanced and an ideal reconstruction (to be defined below) at a set of different signal-to-noise ratios. We compare quality of reconstruction in terms of two performance measures: relative mean squared error ($RMSE$) and percentage of correctly identified support. We introduce the ideal reconstruction to obtain a lower bound on relative mean squared error.

The relative mean squared error is defined as $RMSE = \frac{\|\widehat{\mathbf{s}} - \mathbf{s}_0\|_2^2}{\|\mathbf{s}_0\|_2^2}$, where $\widehat{\mathbf{s}}$ is a solution to an optimization problem, either joint or independent reconstruction, and $\mathbf{s}_0$ is the true underlying object. The second performance measure is a discrepancy between the ground truth support set $T = \text{supp}\{\mathbf{s}_0\}$ and a support set of a reconstructed image $\widehat{T}$. The support set $\widehat{T}$ differs form the true support set T two ways: an algorithm can introduce spurious pixel responses outside of the support set T (false alarms), or it can miss to identify a pixel in the support set T (missed detection). Due to the presence of noise, the set $\widehat{T}$ actually spreads across the whole spatial image. In order to bound the set $\widehat{T}$, one would need to threshold pixel's magnitudes below $\gamma\sigma$ to zero. The parameter γ defines a propagation of the input noise with standard deviation σ into the solution through an optimization algorithm. Instead of following this route further, we resort to a simple measure of the percentage of $|T|$ largest components of the solution $\widehat{\mathbf{s}}$ that belong to the set T.

As a baseline for $RMSE$ comparison, we define the ideal reconstruction as a reconstruction obtained by an algorithm that assumes that a spatial support is available and known at the receiver through an oracle. With the oracle help, one can *a priori* set all pixel values outside the signal support to zero and hand-pick the columns of the operator $\mathbf{\Phi}$ that correspond to pixels carrying the signal. The system reduces to

$$\mathbf{r} = \mathbf{\Phi}_T\mathbf{s}_T + \mathbf{z}$$

where $\boldsymbol{\Phi}_T$ is equivalent to the original matrix $\boldsymbol{\Phi}$ with appropriately pruned columns. The new signal $\mathbf{s}_T$ has the dimension $|T|$, much smaller then the original signal $\mathbf{s}$ dimension N. We also assume that the size of the measurement vector $\mathbf{r}$ is M, such that $M > |T|$. In other words, with the oracle help the problem of tackling the ill-posed inverse problem becomes a classical problem of parameter estimation in Gaussian white noise. The optimal maximum likelihood solution is equivalent to a least squares solution given by:

$$\widehat{\mathbf{s}}_T = (\boldsymbol{\Phi}_T^* \boldsymbol{\Phi}_T)^{-1} \boldsymbol{\Phi}_T^* \mathbf{r}.$$

Its expected mean square error is given by the formula

$$\mathbb{E}\|\widehat{\mathbf{s}}_T - \mathbf{s}_T\|_2^2 = \mathbb{E}\|(\boldsymbol{\Phi}_T^* \boldsymbol{\Phi}_T)^{-1} \boldsymbol{\Phi}_T^* \mathbf{z}\|_2^2 = \sigma^2 Tr((\boldsymbol{\Phi}_T^* \boldsymbol{\Phi}_T)^{-1}), \tag{7}$$

where σ^2 is noise variance and the corresponding $RMSE$ is readily derived.

Clearly the error achieved by the ideal reconstruction is a function of the matrix $\boldsymbol{\Phi}_T$ which in turn depends on the signal itself and number of parameters at which the system operates. Most notably, it depends on the number of measurements per image as well as the width of the viewing aperture corresponding to one image. Additionally, it depends on the distance between spatial pixels, i.e. resolution. Note that although we call this reconstruction ideal because of the oracle assistance, this reconstruction is not optimal in the sense of an achievable minimal mean square error. For the optimal reconstruction one should not assume that estimating on the true support of $\mathbf{s}_0$ achieves the minimal error. This follows by simply noting that if k-th component of the unknown $\mathbf{s}_0$ is such that its response is buried in the noise $|(\mathbf{s}_0)_k| < \gamma\sigma$, the smaller mean square error would be achieved by simply not estimating $(\mathbf{s}_0)_k$, i.e. by setting it to zero.[10] However, the optimal approach quickly becomes computationally intractable since it requires finding a least squares solution to $\mathbf{r} = \boldsymbol{\Phi}_T' \mathbf{s}_T' + \mathbf{z}$ for each set T' with support $T' \subset T$. The optimal reconstruction is then achieved by a LS estimator among the set of LS estimators that has the minimal relative mean square error.

4.2 Synthetic Example

The synthetic example is described as follows. We assume that a scene consists of a set of anisotropic point scatterers, i.e. a set of point scatterers reflecting non-uniformly over different aspect angles. In particular, we construct a synthetic example, pertinent to wide-angle SAR, where we are interested in uncovering a set of lexicographically ordered sparse images with two properties. First, the spatial support of any two consecutive images in the set is highly correlated and second, responses at active pixel locations across the whole set of images have limited persistence. We model an azimuth response of each active pixel as a first order Markov chain with two states: zero response and non-zero response state. Non-zero response state is modeled as a first order autoregressive process. Note that a tacit and important assumption in this study is that each image is sparse. Typical spatial 16×16 pixel reflectivity images are shown in Figure 3. Sparsity of the ground truth image is 5%. Each image corresponds to a sub-aperture of 1°. In each sub-aperture, chirp pulses interrogate the scene with 8 viewing angles and 16 frequencies over 500MHz bandwidth. Thus, we seek to uncover 256 unknown pixel responses of each image with 128 measurements per spatial image. Pixel range and cross-range resolutions are set to 0.3m. From the system parameters the predicted range and cross-range resolutions are 0.3m and 0.85m, respectively. We run the optimization algorithm in both joint processing and independent, point enhanced mode. Regularization parameters are optimized in each mode independently.

In Figure 4 we compare the performance when the set of 20 spatial images is reconstructed by joint processing of all images to the reconstruction of independent-point enhanced processing. In the point-enhanced reconstruction case, the $RMSE$ is calculated by concatenating all separately reconstructed spatial images at different aspects into one vector and applying the $RMSE$ formula. $RMSE$s achieved by these approaches as a function of signal to noise ratio is given in Figure 4(a). Theoretically predicted performance with the oracle assistance is plotted as the baseline for comparison. These results indicate that joint processing of spatial images that have highly correlated spatial support considerably reduces the error over the independent point-enhanced processing and significantly reduces the gap to ideal reconstruction.

An evaluation of the techniques in terms of correctly identified support is given in Figure 4(b). These results indicates that joint processing achieves better noise suppression. This point is further exemplified in Figure 5
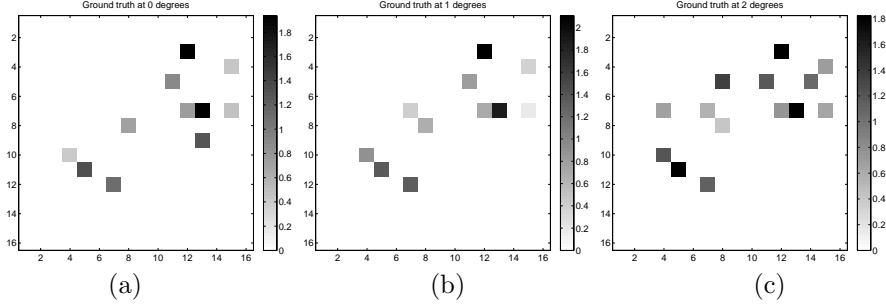
Figure 3. Typical ground truth images at three consecutive aspect angles: (a) 0°, (b) 1° and (c) 2°.
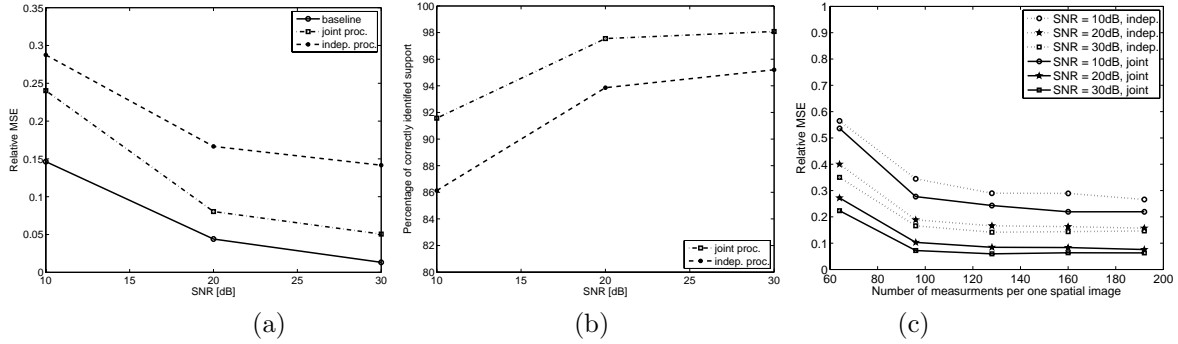

Figure 4. (a) Average relative mean square error as a function of signal to noise ratio (SNR) for 20 Monte Carlo runs with 8 phase history aspects per one spatial image, (b) percentage of correctly identified support and (c) average $RMSE$ sensitivity to number of measurements per one 16×16 spatial image.

where we visually compare different pixel errors when averaged across azimuth. As expected, joint processing strongly suppresses errors outside set T, whereas noise level outside the set T is increased for independent point enhanced processing. Typical anisotropic responses and their reconstructions of several pixels over a full range of 20 aspect angles are shown in Figure 6. Independent reconstruction introduces spurious responses at 'non-active' pixel locations and at times it misses to identify certain azimuth responses. Noise floor of pixels in the set T that have zero response at certain azimuths is typically smaller for the independent reconstruction (the top row of Figure 6). On the other hand, noise floor at pixels in the complement set T^c is smaller for joint processing (the last two figures in the bottom row of Figure 6). This is an expected behavior as joint processing explicitly imposes sparsity on pixels in the set T^c.

In Figure 4(c) we show the SAR sensor matrix sensitivity to reduction in the number of observation aspects. Azimuth returns are subsampled uniformly at random, such there is the same number of measurements in each
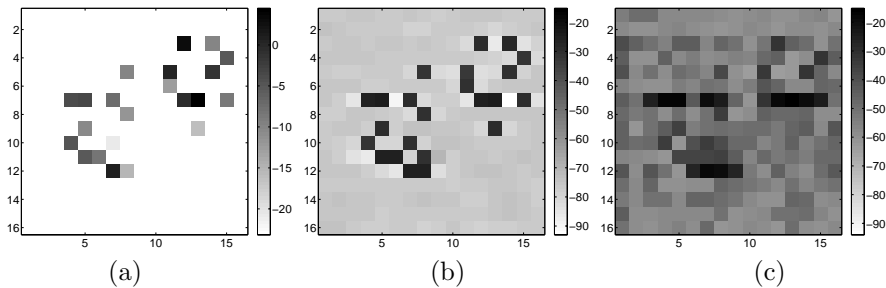

Figure 5. (a) Average spatial magnitude of reflectivity response over azimuth for the sample ground truth, (b) average spatial error over azimuth for joint processing and (c) average spatial error over azimuth for independent processing ($SNR = 20$dB).
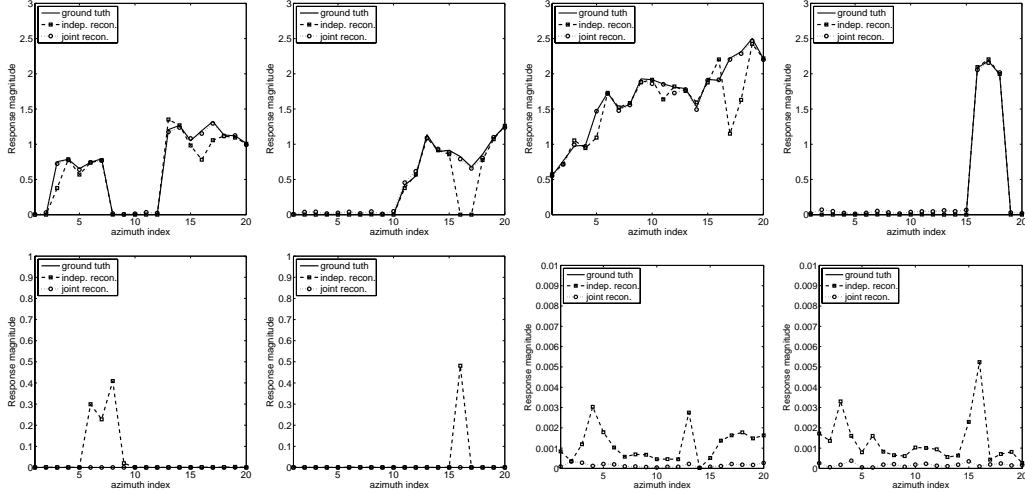
Figure 6. Reflectivity magnitude vs azimuth for several sample pixels in the support set T (top row) and the set T^c (bottom row). Note that pixels in the set T^c have zero true response.

sub-aperture. From a theoretical point of view and under certain assumptions on a linear forward operator, the number of measurements needed to reconstruct a sparse signal is proportional to its support size, rather that its cardinality.[11] The result in Figure 4(c) indicates that SAR forward operator Φ falls into the category of operators that allow for measurement compression, i.e. there is no cost in the achieved $RMSE$ for the wide range of azimuth sub-sampled measurements.

4.3 Backhoe Xpatch data set reconstruction

In this section we present imaging results based on a backhoe dataset, generated by the XPatch simulator.[9] The CAD model of the backhoe is given on Figure 7(a). The phase history data are collected over $\Delta\theta = 110^o$ azimuths in the range $[-10^o, 100^o]$ at 30° elevation, with the frequency bandwidth $B = 500$MHz around the center frequency $f_c = 10$GHz. The reconstruction grid is chosen such that one 128×128 spatial image is reconstructed every 5°. Thus, there are total of 22 jointly reconstructed images corresponding to 22 consecutive, non-overlapping viewing aspects.

First, we apply the traditional polar-format algorithm on phase history over the full range of aspects and reconstruct one image, Figure 7(b). Polar format algorithm is implemented by applying 1-D range resampling, followed by 1-D azimuth resampling.[4] In order to avoid ringing in the spatial domain due to limited bandwidth in spatial frequency (wavenumber) domain, we apply Taylor windowing on the resampled data before taking the 2-D inverse Fourier transform. Taylor window is specified by 4 nearly constant-level sidelobes adjacent to the mainlobe and -35dB sidelobe suppression below the mainlobe level.

Due to visualization constraints we first present a composite WSAR image obtained by independent-point enhanced processing in Figure 7(c) and the composite image obtained by joint processing in Figure 7(d). The composite image is defined as an image of maximum pixel reflectivity magnitudes across all azimuths.[2] This simple metric aims at finding the peak response across all viewing angles of a spatial pixel (x_n, y_n), i.e. $\max\{|s(x_n, y_n, \theta_i)|, i = 1, \ldots, I\}^2$. Note that these images are plotted in dB scale, by first thresholding small values to zero at the same threshold level for both joint and independent reconstructions. The composite image results show the backhoe's reflectivity in much finer detail when compared to results of polar format algorithm applied to the full aperture data. Spatial support of the jointly reconstructed composite image is much smaller and only the dominant features are reconstructed. Independent reconstructions also identify dominant features similarly, however some spurious scatterers appear to be present in the reconstructed image.

Next, in Figure 8 we present magnitudes of the backhoe's spatial reflectivity when viewed from several consecutive reconstruction angles. Joint and independent, point-enhanced processing produce better focused
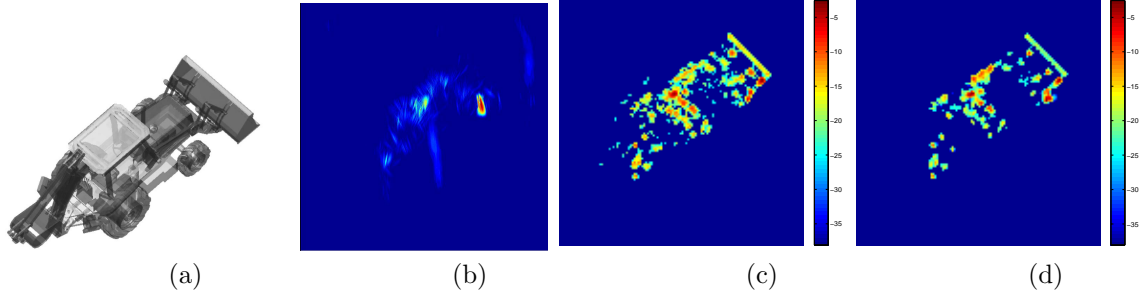
(a)   (b)   (c)   (d)

Figure 7. (a) The backhoe CAD model, (b) polar format algorithm applied on the full aperture of 110° and composite images of (c) independent, point-enhanced reconstruction ($q = .8, \beta = .1$) and (d) joint reconstruction ($p = .8, \alpha = .05, q = .8, \beta = .1$) of 22 images each corresponding to a sub-aperture of 5°.
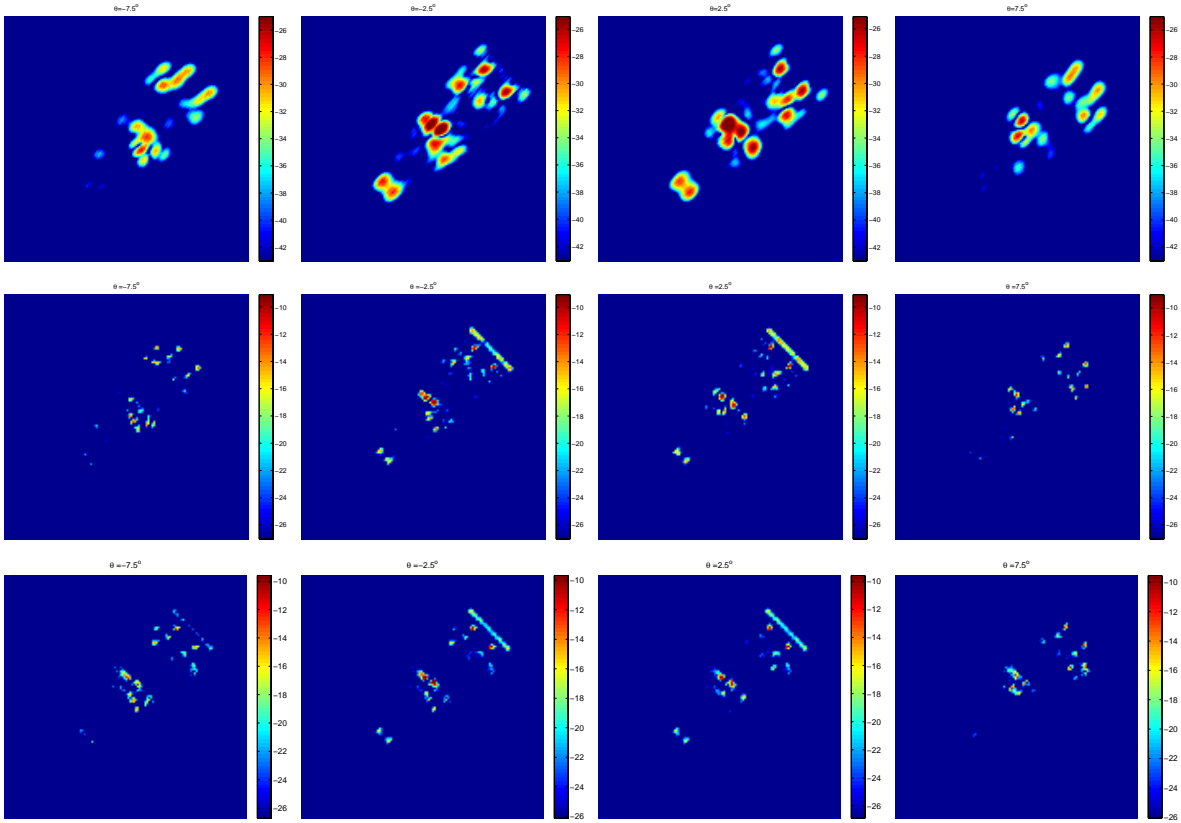

Figure 8. Three sample reconstructed SAR images each of 5° width with maximum number of measurements. Columns left to right correspond to images centered at -7.5^o, -2.5^o, 2.5^o, 7.5^o degrees azimuth. Rows correspond to polar format with Taylor windowing reconstruction (top row), independent (middle row) and joint processing (bottom row).

imagery, whereas a noticeable point spreading is visible at the images reconstructed by the polar format algorithm. Joint and independent reconstructions are plotted on the same dB scale. Independent reconstruction yields larger magnitude responses, i.e. point-enhancing, while joint processing produces images with more compact spatial support. Contrasting independent and joint reconstructions of the first three columns of Figure 8, we see smoother change in reflectivities over angle in the joint processing result.

Figure 9 shows reconstructed reflectivity shapes as a function of azimuth for a set of sample pixels. As expected, reflectivity aspect signature has limited persistence, with high correlation over small aspect extents. The fine detail provided in these plots allows for a scattering center feature extraction. For example, scatterers
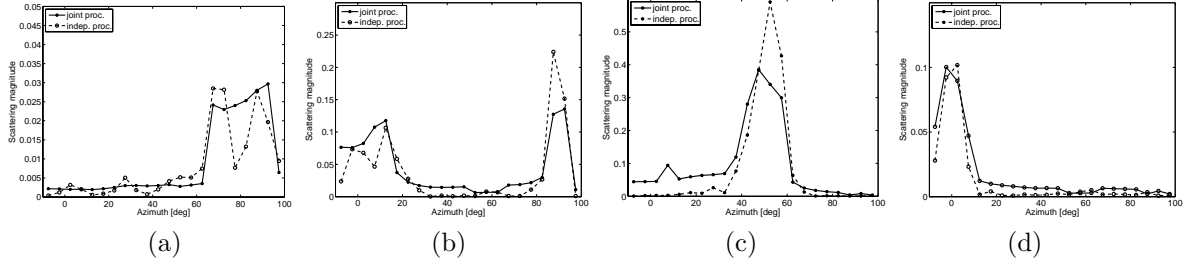
Figure 9. Magnitude of reflectivity response over full range of aspects for several sample pixels.
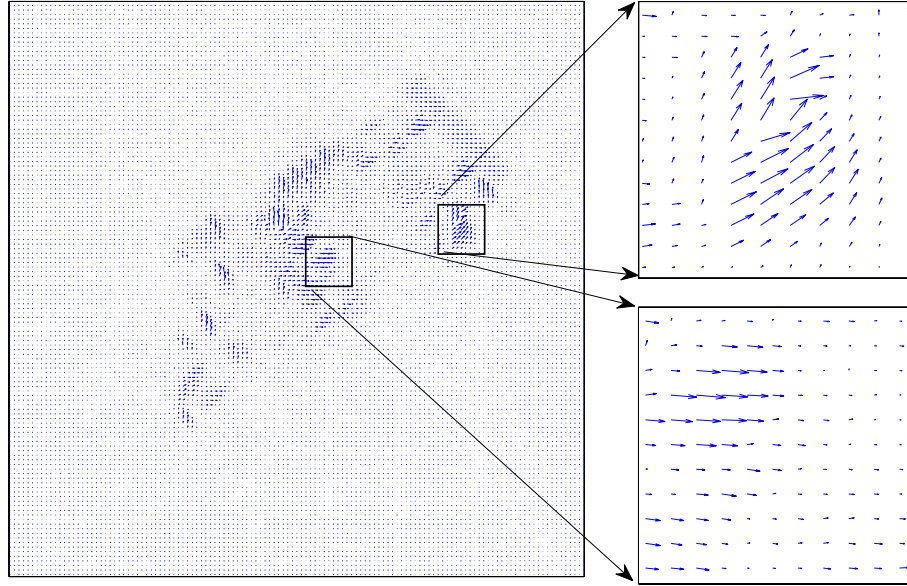

Figure 10. Quiver plot indicating aspect angle of the maximum scattering magnitude response.

such as flat, metal plates have glint anisotropy that is very thin in azimuth, whereas flag and metal poles act as isotropic point scatters. Note that joint processing typically produces smooth scattering shapes, whereas independent processing reconstructs shapes that are jittery. Similarly to the synthetic example, a noise floor in azimuth direction, at point scatterer locations, appears somewhat elevated in the case of joint processing.

In Figure 10 we present a quiver plot indicating aspect angle of the maximum scattering magnitude response.

In Figure 11 we show a set of composite image reconstructions for a sparse collection aperture. In particular, for joint and independent processing the sparse aperture is defined as azimuth subsampled phase history returns. Phase history azimuths within each sub-aperture, i.e. for each image, are chosen uniformly at random among full set of azimuth returns such that each image has equal number of measurements. In contrast, subsampling for the polar format algorithm is performed uniformly, but non-random to aid range and azimuth resampling of the phase history returns. Random downsampling with polar format reconstructions produces much worse results and we omit presenting these plots. We first see that the quality of the composite reflectivity image reconstruction is weakly dependent on the number of azimuth measurements. Joint and independent processing appear more robust when compared to polar format reconstructions. As the subsampling drops down to 35%, independent, point-enhanced processing tends to increase a number of spurious point scatterers , whereas spatial support for joint processing remains focused with further point sharpening.
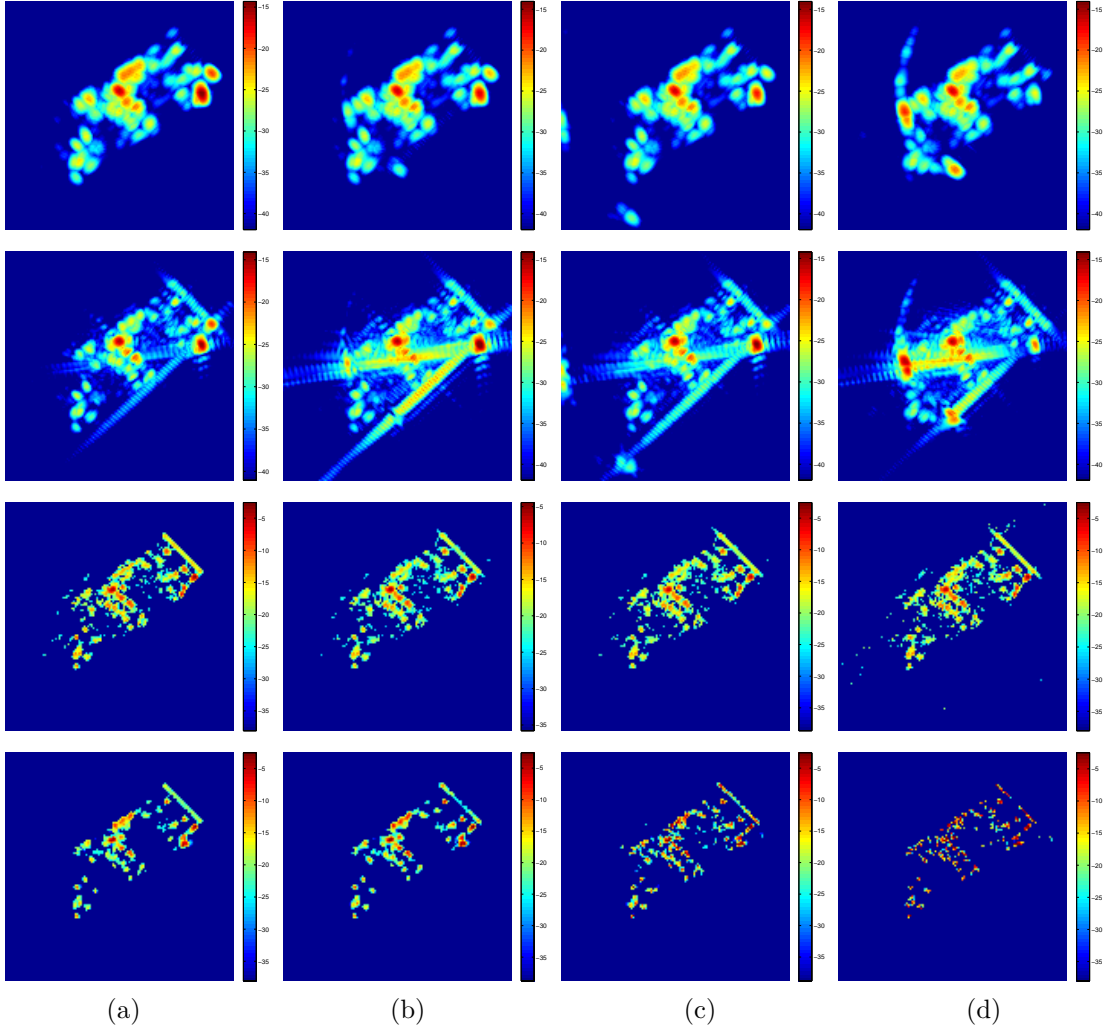
Figure 11. Composite WSAR images with azimuth phase history returns sub-sampled at (a) 100%, (b) 70%, (c) 50% and (d) 35% of the maximum number of available azimuth measurements. Composite images correspond to polar format algorithm with and without Taylor windowing(top two rows), independent, point enhanced processing (third row) and joint processing (bottom row).

5. CONCLUSION

We have approached wide-angle SAR reflectivity reconstruction as a three-dimensional inverse problem exploiting the fact that spatial reflectivity fields are sparse and that their magnitudes are smooth with fast transitions at random aspect angles. This approach allows for anisotropic reflectivity characterization without the need for detailed prior knowledge of azimuth persistence or scattering type. We have shown that this algorithm produces better focused imagery on Xpatch Backhoe data set when compared to traditional polar format algorithm. Algorithms that can finely characterize anisotropy of the scene's reflectivity field, provide a path for moving from pixel-based imaging to object level information extraction. This information can be tied to higher processing blocks that perform e.g. automatic target recognition (ATR). Furthermore, reconstruction quality exhibits robustness to limitations in data quantity, leaving room for a spotlight SAR sensor to multiplex interrogation of more than one ground scene during phase history collection.

APPENDIX A. ALGORITHM

The solution to the minimization problem can be obtain multiple ways and here we present an algorithm based on a quasi-Newton method. For general $0 \le p \le 1$, the l_p norm is non-differentiable around the origin. In the first step, any l_p norm is approximated by a smooth function $\|z\|_p^p \approx \sum_{i=1}^{K} ((z_i)^2 + \epsilon)^{\frac{p}{2}}$. The gradient can be written in compact form:

$$\Delta J_\epsilon(\mathbf{s}) = H(\mathbf{s})\mathbf{s} - 2\mathbf{\Phi}^H \mathbf{r} \tag{8}$$

where Hessian approximation $H(\mathbf{s})$ is given by:

$$H(\mathbf{s}) = 2\mathbf{\Phi}^H \mathbf{\Phi} + p\alpha P^H(\mathbf{s})\mathbf{D}_\theta^T \Lambda_1(\mathbf{s})\mathbf{D}_\theta P(\mathbf{s}) + q\beta\Lambda(\mathbf{s})$$

$$\Lambda_1(\mathbf{s}) = \mathrm{diag}\{\|(\mathbf{D}_\theta|\mathbf{s}|)_k\|^2 + \epsilon)^{p/2-1}\}$$

$$\mathbf{D}_\theta = \mathrm{diag}\{[-I, I]\}$$

$$P(\mathbf{s}) = \mathrm{diag}\{\exp(-j\angle(\mathbf{s})_k)\}$$

$$\Lambda(\mathbf{s}) = \mathrm{diag}\{\mathrm{diag}\{(\sum_{i=1}^{I} |s(x_n, y_n, \theta_i)|^2 + \epsilon)^{q/2-1}\})\}$$

The quasi-Newton solution at iteration m is

$$\widehat{\mathbf{s}}^{(m+1)} = \widehat{\mathbf{s}}^{(m)} - \delta[H(\widehat{\mathbf{s}}^{(m)})]^{-1}\Delta J_\epsilon(\widehat{\mathbf{s}}^{(m)}), \tag{9}$$

where δ controls a size of the quasi-Newton step. Substituting the gradient of the cost function given in Equation 8, the quasi-Newton iteration is given by

$$H(\widehat{\mathbf{s}}^{(m)})\widehat{\mathbf{s}}^{(m+1)} = (1 - \delta)H(\widehat{\mathbf{s}}^{(m)})\widehat{\mathbf{s}}^{(m)} + \delta 2\mathbf{\Phi}^H \mathbf{r}. \tag{10}$$

Note that this a linear set of equations with the unknown $\widehat{\mathbf{s}}^{(m+1)}$ and the right hand side recalculated at each iteration. This system can be solved itself iteratively by for example, a conjugate gradient method.

REFERENCES

[1] Potter, L. C. and Moses, R. L., "Centers for SAR ATR," *IEEE Transactions on Image Processing* (January 1997).

[2] Moses, R. L., Potter, L. C., and Cetin, M., "Wide angle SAR imaging," *SPIE Defense and Security Symposium, Algorithms for Synthetic Aperture Radar Imagery XI* (April 2004).

[3] Varshney, K. R., Cetin, M., FisherIII, J. W., and Willsky, A. S., "Joint image formation and anisotropy characterization in wide-angle SAR," *SPIE Defense and Security Symposium, Algorithms for Synthetic Aperture Radar Imagery XIII* (April 2006).

[4] C.V.Jakowatz, E.Wahl, D., S.Eichel, P., C.Ghiglia, D., and Thompson, P. A., [*Spotlight-mode Synthetic Aperture Radar: a Signal Processing Approach*], Kluwer Academic Publishers, Norwell, MA (1996).

[5] Bertero, M., "Linear inverse and ill-posed problems," *Advances in Electronics and Electron Physics* **75**, 1–120 (1989).

[6] Malioutov, D. M., Cetin, M., and Willsky, A. S., "A sparse signal reconstruction perspective for source localization with sensor array," *IEEE Trans. Signal Processing* **53**, 3010–3022 (August 2005).

[7] Cotter, S. F., Rao, B. D., Kjersti, E., and Kreutz-Delgado, K., "Sparse solutions to linear inverse problems with multiple measurement vectors," *IEEE Transactions on Signal Processing* **53**, 2477 – 2488 (July 2005).

[8] Cetin, M., [*Feature-Enhanced Synthetic Aperture Radar Imaging*], Ph.D. Thesis, Boston University (February 2001).

[9] "Backhoe data sample and visual-d challenge problem," *Air Force Research Laboratory, https://www.sdms.afrl.af.mil/main.htm* .

[10] Donoho, D. L., Johnstone, I. M., Stern, A. S., and Hoch, J. C., "Maximum entropy and the nearly black object," *Journal of the Royal Statistical Society B* **54**, 41–81 (1992).

[11] Candes, E. J., "Compressive sampling," *Int. Congress of Mathematics* **3**, 1433–1452 (2006).